Nanoscale Advances

ROYAL SOCIETY OF CHEMISTRY

PAPER

View Article Online
View Journal | View Issue

Cite this: *Nanoscale Adv.*, 2020, **2**, 4153

Zero-mode waveguides can be made better: fluorescence enhancement with rectangular aluminum nanoapertures from the visible to the deep ultraviolet†

Mikhail Baibakov, Aleksandr Barulin, Prithu Roy, Jean-Benoît Claude, Satyajit Patra and Jérôme Wenger *

Nanoapertures milled in metallic films called zero-mode waveguides (ZMWs) overcome the limitations of classical confocal microscopes by enabling single molecule analysis at micromolar concentrations with improved fluorescence brightness. While the ZMWs have found many applications in single molecule fluorescence studies, their shape has been mainly limited to be circular. Owing to the large parameter space to explore and the lack of guidelines, earlier attempts using more elaborate shapes have led to unclear conclusions whether or not the performance was improved as compared to a circular ZMW. Here, we comparatively analyze the performance of rectangular-shaped nanoapertures milled in aluminum to enhance the fluorescence emission rate of single molecules from the near infrared to the deep ultraviolet. Our new design is based on rational principles taking maximum advantage of the laser linear polarization. While the long edge of the nanorectangle is set to meet the cut-off size for the propagation of light into the nanoaperture, the short edge is reduced to 30 nm to accelerate the photodynamics while maintaining bright fluorescence rates. Our results show that both in the red and in the ultraviolet, the nanorectangles provide 50% brighter photon count rates as compared to the best performing circular ZMWs and achieve fluorescence lifetimes shorter than 300 ps. These findings can be readily used to improve the performance of ZMWs, especially for fast biomolecular dynamics, bright single-photon sources, and ultraviolet plasmonics.

Received 5th May 2020
Accepted 20th July 2020

DOI: 10.1039/d0na00366b

rsc.li/nanoscale-advances

Introduction

The limited spatial resolution of classical confocal microscopes in the hundreds of nanometers restricts the detection of single fluorescent molecules for two main reasons.[1–3] First, the total fluorescence signal collected from a single molecule is bound by the diffraction phenomenon in a homogeneous environment. This is a problem when fast sub-millisecond events need to be probed, requiring high photon count rates.[4,5] Second, the molecules have to be diluted to sub-nanomolar concentrations in order to isolate only a single molecule in the diffraction-limited laser spot. The requirement of low concentrations cannot handle enzymatic reactions, protein–protein or protein–DNA interactions which typically occur at much higher micromolar concentrations in physiological conditions.[1]

To overcome these challenges and improve the detection of single fluorescent molecules at high micromolar concentrations, nanoapertures milled in opaque metallic films with diameters from 50 to 200 nm have been introduced to confine the light at the nanometer scale, and have been termed zero-mode waveguides (ZMWs).[6,7] The metal nanostructure increases the local excitation intensity thanks to the plasmonic enhancement.[8] It also modifies the fluorescence photokinetics decay rates,[9] improving the net detected photon count rate per molecule.[10–20] Moreover, as the aperture diameter is largely below half the optical wavelength, the light exponentially decays inside the nanoaperture,[8] leading to an effective detection volume in the attoliter (10^{-18} L) range, one thousand fold smaller than with a diffraction-limited confocal microscope.[1,6] These improvements have enabled a wide range of applications, including DNA sequencing,[21–23] enzymatic reactions,[13,24,25] protein–protein interactions,[26–30] nanopore detection,[31–36] and biomembrane studies.[37–41]

So far, most studies on zero-mode waveguide nanoapertures consider only circular shapes, as this is an intuitive form which appears also simple to fabricate.[42–44] Few reports have considered non-circular aperture shapes such as rectangles,[45–50] triangles,[51,52] bowties,[53,54] C- or H-apertures.[55,56] While these more advanced shapes offer more parameters to tune the

Aix Marseille Univ, CNRS, Centrale Marseille, Institut Fresnel, 13013 Marseille, France. E-mail: jerome.wenger@fresnel.fr

† Electronic supplementary information (ESI) available: Influence of the milling depth, single molecule fluorescence time traces in circular ZMWs. See DOI: 10.1039/d0na00366b

nanoaperture response, in the absence of clear guidelines the parameter space to explore becomes also larger, and the performance gain as compared to a circular nanoaperture is often unclear or marginal. Achieving the brightest emission rate together with short fluorescence lifetimes is important for applications on fast biomolecular dynamics,[4,5] single-photon sources,[14] and also for the newly-developing field of ultraviolet plasmonics.[57–62]

Here we rationally explore the use of rectangular-shaped nanoapertures milled in aluminum to enhance the fluorescence emission rate of single molecules from the near infrared (excitation 635 nm, detection 655 to 755 nm) down to the deep ultraviolet (excitation 266 nm, detection 310 to 410 nm). We use aluminum layers with optimized deposition parameters,[63,64] as the response for gold films falls below 600 nm and hence gold films cannot be used efficiently for dyes with emission from the green to the ultraviolet.[65] The rationale behind our aluminum nanorectangle design is based on the fact that for a linearly polarized incoming light, the propagation constant inside the nanoaperture is mainly set by the aperture dimension in the direction perpendicular to the laser polarization.[8] As for a circular ZMW, the aperture dimension along this direction has to be around the cut-off size to maximize the local intensity gain and the quantum yield enhancement. The aperture dimension along the other direction (parallel to the laser polarization) can be made as short as 30 nm to take maximum advantage of the plasmonic enhancement and accelerate the emission photodynamics. Quite strangely, despite the large interest for zero-mode waveguide nanoapertures, this simple configuration was never tested before.[45–49] Here, we go one step further by exploring the design parameter space, quantitatively assessing the performance as compared to circular nanoapertures of optimized dimensions and maximizing the fluorescence enhancement for UV plasmonics.

Results

Circular and rectangular nanoapertures are milled using focused ion beam (FIB) on the same aluminum layers deposited microscope coverslips (Fig. 1a and b). The design is guided as the long edge of the nanorectangle (NR) should correspond to the cut-off size for the propagation of the fundamental mode inside the aperture. For rectangular apertures milled in a perfect electrical conductor, the theoretical cut-off size is $0.5\ \lambda/n$ where n is the refractive index of the medium filling the aperture (for a circular aperture, the cut-off diameter is $0.59\ \lambda/n$).[8] For real metals, the cut-off dimension is slightly shorter as some part of the electromagnetic field penetrates into the metal.[47] From experiments on circular nanoapertures milled in aluminum, we know that the optimum size for experiments in the visible spectral range is about 110 nm,[20] while it amounts to 60–70 nm for the UV.[60] The other dimension is then made as small as 30 nm to maximize the plasmonic coupling between the two long edges of the NR aperture.[45] Please note that the milling depths in the substrate is optimized as well following earlier works,[19,27] see Fig. S1 in the ESI.†

The numerical simulations indicate that for a $120 \times 30\ nm^2$ NR, the local intensity enhancement can be higher than 30× (Fig. 1c), about 8 times higher than for a circular ZMW of optimized diameter (Fig. 1e). Slight deviations from the optimum size tend to decrease the intensity enhancement: for a $100 \times 30\ nm^2$ NR, the enhancement is about twice lower at

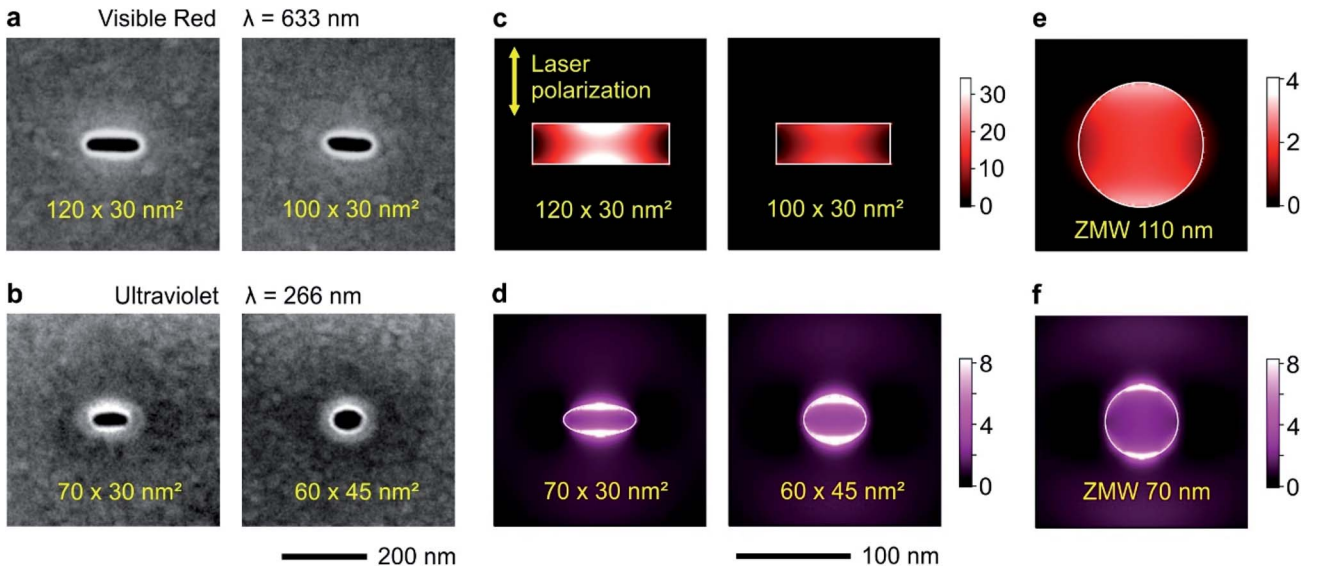

Fig. 1 Nanorectangle (NR) apertures milled in an aluminum film to concentrate the light at a subwavelength scale. (a and b) Scanning electron microscope image of some NR samples tested for the visible and UV experiments. All images have the same scale and $500 \times 500\ nm^2$ total dimensions. (c–f) Numerical simulations using finite-difference time-domain method of the electric field intensity enhancement within a plane located 10 nm inside the aperture (red wavelength (c and e)) or 5 nm (ultraviolet, (d and f)). Circular zero-mode waveguide (ZMW) apertures are shown in (e and f) to serve as reference. Throughout (c–f), the incoming light polarization is oriented vertically and perpendicular to the long axis of the NR.

15×, but still higher than the circular ZMW. The same conclusions still hold in the UV (Fig. 1d and f): while the average intensity enhancement for a circular ZMW is about 3.5×, it increases to 5.6× for a 60 × 45 nm^2 NR and 6.0× for a 70 × 30 nm NR. Due to the short UV wavelength, achieving even higher local intensity enhancement values would require NR widths of about 10 nm, which are presently challenging to achieve using FIB.

To verify experimentally these predictions and quantify the performance of nanorectangles to enhance the fluorescence of single molecules, we start by performing experiments in the red spectral range. The fluorescent dyes are Alexa Fluor 647, which do not adsorb on the aluminum surface and enable accurate quantification of the aperture influence.[66] The excitation is 635 nm and the collection is performed in the 655–755 nm window (Fig. 2a). Single NR and ZMWs are covered with the solution at 2.8 μM concentration of Alexa Fluor 647. Fluorescence correlation spectroscopy (FCS) and fluorescence lifetime data are then recorded for individual apertures while the fluorescent molecules are constantly diffusing across the aperture volume. Fig. 2b shows the raw and the normalized FCS correlation functions inside a 120 × 30 nm^2 NR and a 110 nm diameter circular ZMW.

The FCS analysis quantifies various parameters: the average number of molecules, their diffusion time across the aperture and their fluorescence brightness (see Methods section). All the fit results for Fig. 2b are summarized in Table 2. Comparing the NR to the ZMW, we observe a lower number of molecules indicating a smaller detection volume. This feature is confirmed independently by the shorter diffusion time of 8 μs in the NR as compared to 25 μs in the ZMW. Moreover, the fluorescence count rate per molecule (CRM) is 1.5× brighter in the NR as compared to the ZMW, leading to a 18× fluorescence enhancement inside the NR as compared to the confocal reference (Fig. 2d).

To complement the fluorescence brightness enhancement, another important figure of merit is the fluorescence lifetime reduction. For a circular ZMW, 3× shorter lifetimes can be achieved for diameters below 80 nm, but this comes at the expense of higher quenching losses and lower fluorescence count rates, nearly losing the fluorescence enhancement. While preserving the maximum fluorescence brightness on ZMWs, the lifetime reduction is typically about 2×. On the contrary, NRs allow to achieve faster photoemission dynamics (Fig. 2c) and 3.6× reduction in the fluorescence lifetime without compromising on the fluorescence brightness (Fig. 2e and Table 2). Importantly, Fig. 2 shows that for red fluorescent dyes, the NR apertures outperform the circular ZMWs by providing brighter emission rates and faster fluorescence lifetimes. We have also checked these features for green fluorescent dyes Alexa Fluor 546 excited at 557 nm and confirmed the results obtained in the red spectral range. While all these results have been obtained on diffusing molecules and FCS analysis, we confirm the validity of our conclusions by recording fluorescence time traces on immobilized single molecules (ESI Section S2†). Both FCS and single molecule approaches converge towards similar values for the fluorescence brightness enhancement and

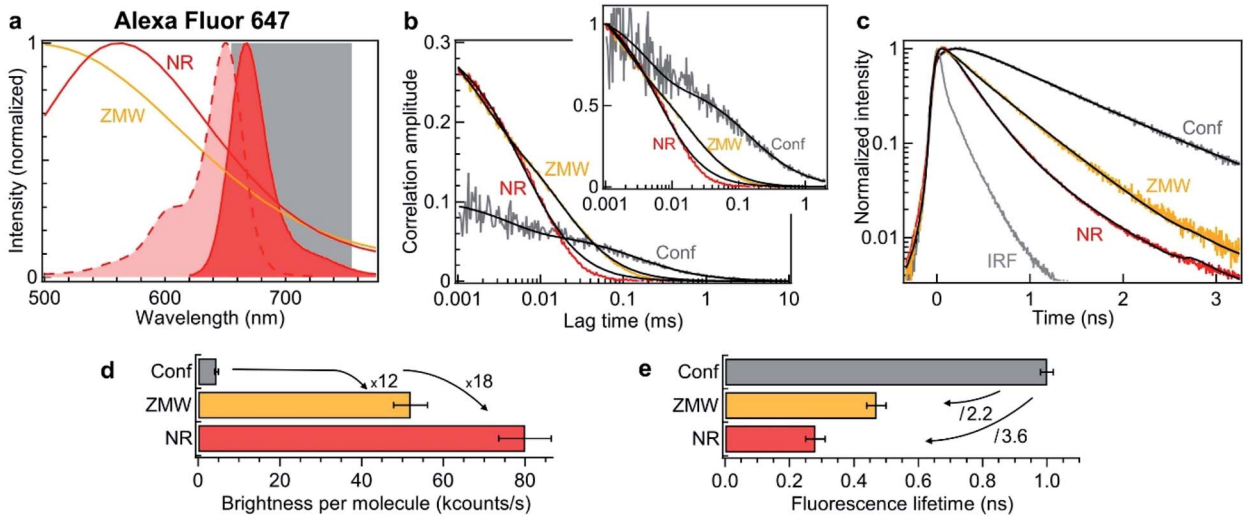

Fig. 2 Nanorectangle (NR) performance comparison with a circular zero-mode waveguide (ZMW) nanoaperture for the red fluorescent dye Alexa Fluor 647. Here the NR size is 120 × 30 nm^2 and the ZMW diameter is 110 nm. Both are milled in the same 100 nm thick aluminum layer deposited on a borosilicate glass substrate. (a) Absorption and emission spectra of Alexa Fluor 647 (shaded curves). The curves for the ZMW and NR are the computed intensity transmission spectra (normalized at by the peak transmission). The 655–755 nm region used for fluorescence collection is indicated. (b) FCS correlation traces for the NR and ZMW taken at 2.8 μM Alexa concentration. The confocal reference data is recorded at 15 nM. The insert shows the amplitude-normalized correlations, indicating a clear shortening of the diffusion time in the NR. Black lines are numerical fits; the results are summarized in Table 1. (c) Fluorescence lifetime decay traces for the different cases, together with the instrument response function (IRF). Again, the black lines are numerical fits; the results are summarized in Table 2. (d) Average brightness per molecule measured by dividing the average fluorescence intensity by the number of molecules monitored by FCS in (b). (e) Fluorescence lifetime extracted from the data fits in (c). For the ZMW and the NR, a biexponential fit is used and the intensity-averaged lifetime is shown.

Table 1 Fit results for the FCS data in Fig. 2b. The Alexa Fluor 647 concentration for the NR and ZMW is 2.8 μM, while it is 15 nM for the confocal case. The excitation power is 20 μW at 633 nm. F is the total fluorescence intensity and CRM = F/N is the fluorescence brightness per molecule. The background is neglected here as it is negligible as compared to the fluorescence signal

	N	τ_d (μs)	T_{ds}	τ_{ds} (μs)	F (kHz)	CRM (kHz)
Confocal	16	140	0.41	4	72	4.5
ZWM 110 nm	4.2	25	0.36	1.7	219	52
NR 120 × 30 nm^2	3.0	8.3	0.06	2	239	80

Table 2 Fit results for the TCSPC data acquired on Alexa Fluor 647 in Fig. 2c. A single exponential fit is used for the confocal while a biexponential fit provides a better fit for the ZMW and the NR. I_i are the relative intensities of each component and τ_{avg} denotes the intensity-averaged lifetime

	τ_1 (ns)	τ_2 (ns)	I_1	I_2	τ_{avg} (ns)
Confocal	1.0	—	1	—	1.0
ZWM 110 nm	0.12	0.55	0.2	0.8	0.47
NR 120 × 30 nm^2	0.15	0.6	0.7	0.3	0.28

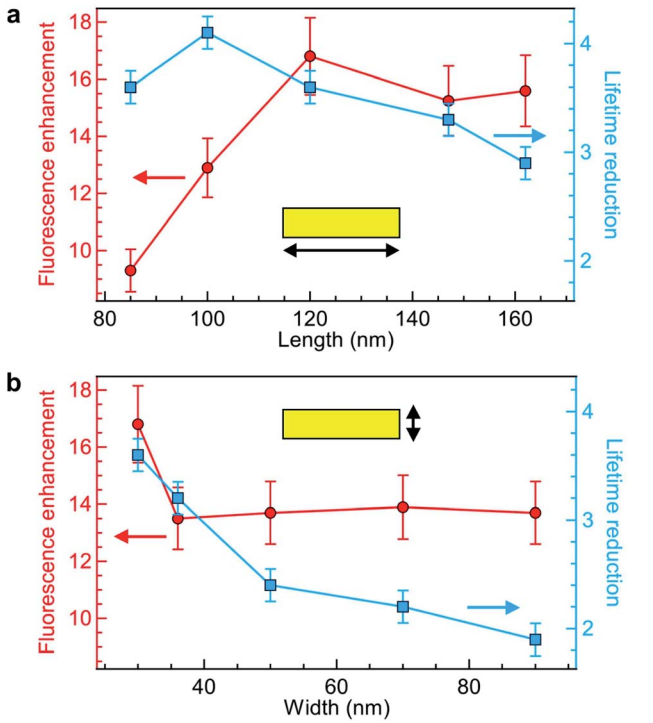

Fig. 3 Exploration of the NR length (a) and width (b) influence on the experimental enhancement of the brightness per Alexa Fluor 647 molecule (red disks, left axis) and the fluorescence lifetime reduction (blue squares, right axis). In (a) the NR width is constant at 30 nm while in (b) the length is constant at 120 nm.

lifetime reduction. Lastly, the excitation power dependence is reported in the ESI Fig. S6.†

Keeping the fluorescence brightness enhancement and the lifetime reduction as two important figures of merit, we explore the influence of the NR length and width (Fig. 3a and b). The experimental conditions are identical to those of Fig. 2 with Alexa Fluor 647 excited at 635 nm. As indicated by the numerical simulations (Fig. 1c), the NR length plays a key role in setting the fluorescence brightness enhancement, with an optimum value at 120 nm for 635 nm wavelength which corresponds to the cut-off size for the propagation of 635 nm light into the NR. The fluorescence lifetime also depends on the NR length, but more moderately as the lifetime reduction stays in the 3–4× range while the NR length is varied from 85 to 160 nm (Fig. 3a). On the contrary, changing the NR width only affects the fluorescence enhancement for the smallest 30 nm value (Fig. 3b) while for all other widths the brightness is nearly constant. The fluorescence lifetime shows a more pronounced dependence with the NR width as this controls the proximity from the fluorescent dye to the metal: the lifetime is significantly reduced for smaller widths. Altogether from the parameter space exploration in Fig. 3 (and other ESI† not shown), we confirm the rationale behind the NR design: the NR length determines mainly the fluorescence enhancement and should be set close to the cut-off condition, while the NR width sets the fluorescence lifetime reduction which should be as small as possible in the 20 to 30 nm range. Due to nanofabrication difficulties, we could not explore NR widths smaller than 30 nm. However, an optimum must exist for this parameter also as if for instance we consider a 10 nm width, the fluorescent dye is always at less than 5 nm from the metal and then strong fluorescence quenching is expected.[67]

Comparing our results in Fig. 3 with earlier works on rectangular nanoapertures, fluorescence enhancement factors in the range from 10 to 25 were found for gold films featuring an additional aluminum layer on top,[49] or 3 to 10 for gold films featuring an additional silicon layer on at the bottom.[50] Previously studied aluminum layers only provided only a moderate 1.3× fluorescence increase,[49] but the comparison is difficult as the aluminum deposition parameters critically influence on the material plasmonic response.[63] In all cases, the fluorescence lifetime reduction remained below 2.5×, while we achieve now higher values up to 4-fold without compromising on the fluorescence brightness.

Using the information obtained in the red region of the spectrum, we now turn to explore the NR performance in the UV range, using deep UV 266 nm excitation and 310–410 nm fluorescence collection. The fluorescent dye used here is *p*-terphenyl, which has a quantum yield of 93% in cyclohexane,[68] with absorption and emission spectra matching the UV range (Fig. 4a). As compared to Alexa Fluor 647 which has an extinction coefficient of 170 000 cm^{-1} M^{-1} at 635 nm, the extinction coefficient of *p*-terphenyl at 266 nm is 5.6× less with 30 400 cm^{-1} M^{-1}. Due to the limited availability of aberration-corrected microscope objectives in the UV, the numerical aperture (NA) used with *p*-terphenyl is only 0.6 while a 1.2 NA was used in the visible. The transmission of UV objectives is also lower with typically 30% transmission while microscope objectives in the visible range achieve transmission higher than 70%. Altogether, and taking into account the higher 200 μW power used in the UV, the brightness expected per *p*-terphenyl molecule in the UV

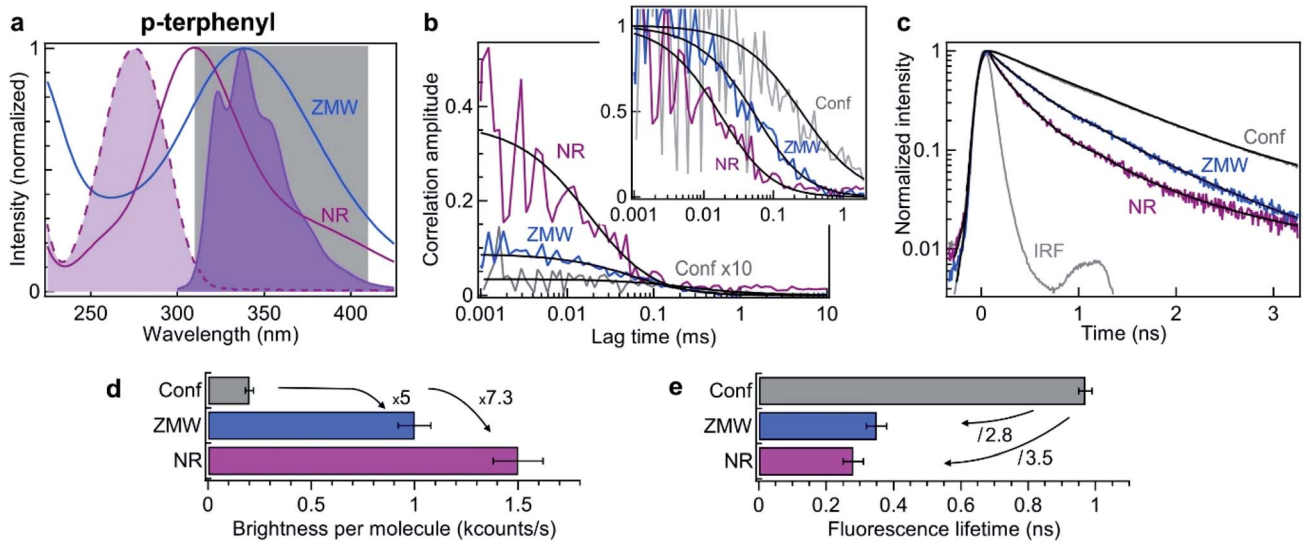

Fig. 4 Nanorectangle (NR) performance comparison with a circular zero-mode waveguide (ZMW) nanoaperture for the UV fluorescent dye *p*-terphenyl. Here the NR size is 60 × 45 nm^2 and the ZMW diameter is 70 nm. Both are milled in the same 50 nm thick aluminum layer deposited on quartz substrate. (a) Absorption and emission spectra of *p*-terphenyl (shaded curves). The curves for the ZMW and NR indicate their computed transmission spectra (normalized at by the peak transmission). The 310–410 nm region used for fluorescence collection is indicated. (b) FCS correlation traces for the NR and ZMW taken at 10 μM concentration in ethanol solution with 40% glycerol. The confocal reference data is recorded at 290 nM and multiplied by 10 for clarity. The insert shows the amplitude-normalized correlations, indicating a clear shortening of the diffusion time in the NR. Black lines are numerical fits; the results are summarized in Table 3. (c) Fluorescence lifetime decay traces for the different cases, together with the instrument response function (IRF). Again, the black lines are numerical fits; the results are summarized in Table 4. (d) Average brightness per molecule measured by dividing the average fluorescence intensity by the number of molecules monitored by FCS in (b). (e) Fluorescence lifetime extracted from the data fits in (c). For the ZMW and the NR, the lifetime of the second component is shown as it is the one representative of the nanostructure influence.

Table 3 Fit results for the FCS data acquired on *p*-terphenyl in Fig. 4b. The concentration for the NR and ZMW is 10 μM, while it is 200 nM for the confocal case. The solvent is ethanol with 40% glycerol. The excitation power is 200 μW at 266 nm. Due to the larger noise on the FCS correlation, the triplet blinking (T_{ds} and τ_{ds}) is not considered in the fit

	N	τ_d (μs)	F (kHz)	B (kHz)	CRM (kHz)
Confocal	290	250	56.2	0.4	0.2
ZWM 70 nm	8.7	86	10.3	1.5	1.0
NR 60 × 45 nm^2	0.9	27	2.3	1.0	1.5

is about 20× lower than for Alexa Fluor 647 (comparing the confocal results in Fig. 2, 4, Tables 1 and 3, we retrieve this attenuation value). This calculation shows that despite the best currently available optical components are used in the UV, the brightness per molecule will be low. This highlights the major interest brought by UV plasmonics to enhance this low fluorescence brightness.

Similar experiments to those displayed on Fig. 2 are conducted in the UV using 10 μM solution of *p*-terphenyl diluted in ethanol with 40% glycerol to slow down the diffusion. Fig. 4b shows the raw and the normalized FCS correlation functions inside a 60 × 45 nm^2 NR and a 70 nm diameter circular ZMW. Despite our best attempts, we could not record useful data on the NRs with smaller widths, we suspect some UV-induced photopolymerization occurring preferentially in the narrow width NRs which would disturb our FCS measurements. However, the numerical simulations (Fig. 1d) already indicate that 60 × 45 nm^2 NR provides a better performance than a circular ZMW. The FCS analysis reveals a higher amplitude for the NR as compared to the ZMW, indicating a lower number of molecules and a smaller detection volume. All the fit results for Fig. 4b are summarized in Table 3. As for Alexa 647 dyes, this feature is confirmed independently by the shorter diffusion time of 27 ± 5 μs for *p*-terphenyl in the NR as compared to 86 ± 10 μs in the ZMW (Table 3). Importantly, the fluorescence count rate per molecule (CRM) is 1.5× brighter in the NR as compared to the ZMW, leading to the highest 7.3× fluorescence enhancement inside the NR as compared to the confocal reference (Fig. 4d).

In addition to the FCS data, we investigate the fluorescence lifetime decays (Fig. 4c). Both Alexa Fluor 647 and *p*-terphenyl have a fluorescence lifetime of about 1 ns in homogeneous medium making the comparison between them quite straightforward. As for Alexa 647, we find that the emission dynamics of *p*-terphenyl are further accelerated inside the NR as compared to the ZMW (Fig. 4c) with 3.5× reduction in the fluorescence lifetime inside the NR without compromising on the fluorescence brightness (Fig. 4e). All lifetime fit results in the UV are summarized in Table 4.

Altogether, the data in Fig. 4 confirms in the UV the superior performance of rectangular nanoapertures as compared to their circular counterparts. The design concepts derived from the visible experiments remain valid even down to 266 nm. The

Table 4 Fit results for the TCSPC data acquired on *p*-terphenyl in Fig. 4c. For the confocal case, we use a bi-exponential fit with a 10 ps (fixed) component to account for the scatter noise. For the ZMW and the NR, we add a supplementary component to obtain a better fit. I_i are the relative intensities of each component and τ_{avg} denotes the intensity-averaged lifetime

	τ_1 (ns)	τ_2 (ns)	τ_3 (ns)	I_1	I_2	I_3	τ_{avg} (ns)
Confocal	0.01	0.97	—	0.06	0.94	—	0.91
ZWM 70 nm	0.01	0.35	0.91	0.14	0.28	0.57	0.62
NR 60 × 45 nm^2	0.01	0.28	0.91	0.26	0.38	0.36	0.43

results are fully scalable and in line with the observations in the red spectral range demonstrating an extended optical characterization from the deep UV to the near infrared.

Conclusions

As compared to conventional circular ZMWs, nanorectangle apertures open new possibilities to achieve brighter fluorescence emission, faster lifetime and smaller detection volume. What previously required a compromise with circular ZMWs (reducing the diameter to achieve small volumes and short lifetimes but at the expense of low photon count rates) can now be obtained simultaneously with an even improved fashion with nanorectangles. We have shown that in the red and in the ultraviolet, NRs provide about 50% brighter photon count rates together with lifetimes shorter than 300 ps. The design principle based on aluminum film holds from the near infrared down to the deep UV, taking maximum advantage of the laser linear polarization. The long edge of the NR (perpendicular to the laser polarization) has to be around the cut-off size to maximize the local intensity gain. The short edge of the NR (parallel to the laser polarization) can be reduced to 30 nm to accelerate the emission photodynamics while maintaining bright emission. These results find application in improving the performance of ZMWs for single molecule analysis at high concentrations, and are especially relevant for monitoring fast biomolecular dynamics,[4,5] realizing ultrafast single-photon sources,[14] and for interrogating molecules with ultraviolet plasmonics.[57–62]

Methods

Nanorectangle apertures fabrication

An opaque layer of aluminum is deposited by electron-beam evaporation (Bühler Syrus Pro 710) at a 10 nm s^{-1} rate and a chamber pressure of 5 ×10^{-7} mbar. For the visible experiments, we use 100 nm thickness on borosilicate glass microscope coverslip, while for UV experiments we use 50 nm aluminum thickness on quartz microscope coverslips. The nanorectangle apertures are then milled using a gallium-based focused ion beam (FEI dual beam DB 235 Strata) with 30 kV voltage and 10 pA current.

Visible microscope

The experiments performed on Alexa Fluor 647 dyes in the visible spectral range use a custom build confocal microscope described in ref. 20. A LDH series laser diode (PicoQuant, pulse duration ~50 ps, 40 MHz repetition rate) is used to excite the molecules at 635 nm with a laser power below 20 μW measured at the microscope entrance port. The laser light is focused by a Zeiss C-Apochromat 63×, 1.2 NA water immersion objective, and the fluorescence is collected by the same objective. A 3-axis piezoelectric stage (Physik Instrumente P-517.3CD) is used to place single nanoapertures on the laser focus spot. A dichroic mirror (ZT 405/488/561/640rpc, Chroma) and an emission filter (ZET405/488/565/640mv2, Chroma) filter the fluorescence light. The detection is performed after a 50 μm pinhole conjugated to the object plane. We use an avalanche photodiodes in single photon counting mode (MPD-5CTC with <50 ps timing jitter, Picoquant). The photodiode output is recorded with a time correlated single photon counting module (HydraHarp 400, Picoquant) featuring 110 ps overall temporal resolution.

Ultraviolet microscope

The experiments performed on *p*-terphenyl dyes in the ultraviolet use a custom build confocal microscope described in ref. 60. A 266 nm picosecond laser (Picoquant LDH-P-FA-266, 70 ps pulse duration, 80 MHz repetition rate) is used with a laser power up to 200 μW at the microscope entrance port. The laser light is focused by a Zeiss Ultrafluar 40×, 0.6 NA glycerin immersion objective, and the fluorescence is collected by the same objective. A dichroic mirror (Semrock FF310-Di01-25-D) and two emission filters (Semrock FF01-300/LP-25 and Semrock FF01-375/110-25) filter the fluorescence light. The detection is performed by a single photon counting photomultiplier tube (Picoquant PMA 175) after a 50 μm pinhole conjugated to the object plane. The photomultiplier tube output is recorded with a time correlated single photon counting module (Picoharp 300, Picoquant) featuring 150 ps overall temporal resolution.

FCS analysis

All fluorescence traces are analyzed using Symphotime 64 software (Picoquant). As in our previous works,[12,20,60] we fit the FCS correlation functions with a standard Brownian diffusion model taking into account the background fluorescence level and the photoblinking:[69,70]

$$G(\tau) = \frac{1}{N}\left[1 - \frac{B}{F}\right]^2 \left[1 + \frac{T_{ds}}{1 - T_{ds}} \exp\left(-\frac{\tau}{\tau_{ds}}\right)\right] \left(1 + \frac{\tau}{\tau_d}\right)^{-1} \left(1 + \frac{1}{\kappa^2}\frac{\tau}{\tau_d}\right)^{-0.5} \quad (1)$$

where N is the total number of molecules, B the background noise intensity, F the total fluorescence intensity, T_{ds} the fraction of dyes in the dark state, τ_{ds} the dark state blinking time, τ_d the mean diffusion time and κ the aspect ratio of the axial to transversal dimensions of the detection volume ($\kappa = 5$ for the confocal case and $\kappa = 1$ for the circular and rectangular nanoapertures). This model describes correctly the FCS data inside the nanoapertures without requiring more advanced approaches. It has the advantage of being simple and fully analytical, enabling a direct comparison between the

experiments. As observed previously,[12,20,60] the main residual difference between data and fit concerns the long tail of the FCS function twice larger than the diffusion time, yet this part of the FCS data does not significantly affect our estimations of the number of molecules and mean diffusion time.

Fluorescence lifetime analysis

The fluorescence decay histograms are fitted using Picoquant SymPhoTime 64 sofware with an iterative reconvolution fit considering the instrument response function (IRF). The fits always consider more that 95% of the total collected photons in the region of interest. All the fit parameters are summarized in Tables 2 and 4. For Alexa Fluor 647, the data for the confocal reference is fitted with a single exponential decay, while for the nanoapertures a biexponential function provides a better fit. While the signal to background is excellent in the visible, for the UV experiments we decide to include a supplementary component with fixed 10 ps lifetime to account for the laser scattering and the metal photoluminescence. For UV experiments, we also observe that the long decay tail has a 0.91 ns lifetime similar to the lifetime of *p*-terphenyl in the confocal homogeneous environment. This contribution is likely to stem from a residual emission from molecules lying away from the aperture which do not experience the near-field enhancement from the plasmonic nanostructure. Therefore, in the analysis of Fig. 4e, we decide to focus on the central component which represents essentially the nanoaperture contribution.

Numerical simulations

The intensity distributions displayed on Fig. 1c–f are computed using finite-difference time-domain (FDTD) method with RSoft Fullwave software. The simulated geometry accounts for the fabricated nanorectangles dimensions (Fig. 1a and b). The simulations are run with 0.5 nm mesh size for the UV (1 nm for the visible) and are checked for convergence after more than ten optical periods. The real and imaginary parts of aluminum permittivity are taken from ref. 64, the other refractive indexes are taken from ref. 71.

Funding sources

This project has received funding from the European Research Council (ERC) under the European Union's Horizon 2020 research and innovation programme (grant agreement 723241) and from the Agence Nationale de la Recherche (ANR) under grant agreement ANR-17-CE09-0026-01.

Conflicts of interest

The authors declare no competing financial interest.

References

1 P. Holzmeister, G. P. Acuna, D. Grohmann and P. Tinnefeld, *Chem. Soc. Rev.*, 2014, **43**, 1014–1028.
2 D. Punj, P. Ghenuche, S. B. Moparthi, J. de Torres, V. Grigoriev, H. Rigneault and J. Wenger, *Wiley Interdiscip. Rev.: Nanomed. Nanobiotechnol.*, 2014, **6**, 268–282.
3 E. D. Fabrizio, S. Schlücker, J. Wenger, R. Regmi, H. Rigneault, G. Calafiore, M. West, S. Cabrini, M. Fleischer, N. F. van Hulst, M. F. Garcia-Parajo, A. Pucci, D. Cojoc, C. A. E. Hauser and M. Ni, *J. Opt.*, 2016, **18**, 063003.
4 B. Schuler and H. Hofmann, *Curr. Opin. Struct. Biol.*, 2013, **23**, 36–47.
5 A. Soranno, B. Buchli, D. Nettels, R. R. Cheng, S. Müller-Späth, S. H. Pfeil, A. Hoffmann, E. A. Lipman, D. E. Makarov and B. Schuler, *Proc. Natl. Acad. Sci. U. S. A.*, 2012, **109**, 17800–17806.
6 M. J. Levene, J. Korlach, S. W. Turner, M. Foquet, H. G. Craighead and W. W. Webb, *Science*, 2003, **299**, 682–686.
7 P. Zhu and H. G. Craighead, *Annu. Rev. Biophys.*, 2012, **41**, 269–293.
8 F. J. Garcia-Vidal, L. Martin-Moreno, T. W. Ebbesen and L. Kuipers, *Rev. Mod. Phys.*, 2010, **82**, 729–787.
9 V. V. Klimov, *Phys. Rev. Appl.*, 2019, **12**, 014049.
10 Y. Liu and S. Blair, *Opt. Lett.*, 2003, **28**, 507–509.
11 H. Rigneault, J. Capoulade, J. Dintinger, J. Wenger, N. Bonod, E. Popov, T. W. Ebbesen and P.-F. Lenne, *Phys. Rev. Lett.*, 2005, **95**, 117401.
12 J. Wenger, D. Gérard, J. Dintinger, O. Mahboub, N. Bonod, E. Popov, T. W. Ebbesen and H. Rigneault, *Opt. Express*, 2008, **16**, 3008–3020.
13 J. Wenger, D. Gérard, H. Aouani, H. Rigneault, B. Lowder, S. Blair, E. Devaux and T. W. Ebbesen, *Anal. Chem.*, 2009, **81**, 834–839.
14 J. T. Choy, B. J. M. Hausmann, T. M. Babinec, I. Bulu, M. Khan, P. Maletinsky, A. Yacoby and M. Lončar, *Nat. Photonics*, 2011, **5**, 738–743.
15 X. Jiao, E. M. Peterson, J. M. Harris and S. Blair, *ACS Photonics*, 2014, **1**, 1270–1277.
16 E. Pibiri, P. Holzmeister, B. Lalkens, G. P. Acuna and P. Tinnefeld, *Nano Lett.*, 2014, **14**, 3499–3503.
17 M. S. Alam, F. Karim and C. Zhao, *Nanoscale*, 2016, **8**, 9480–9487.
18 W. E. Martin, B. R. Srijanto, C. P. Collier, T. Vosch and C. I. Richards, *J. Phys. Chem. A*, 2016, **120**, 6719–6727.
19 M. Wu, W. Liu, J. Hu, Z. Zhong, T. Rujiralai, L. Zhou, X. Cai and J. Ma, *Opt. Express*, 2019, **27**, 19002–19018.
20 M. Baibakov, S. Patra, J.-B. Claude, A. Moreau, J. Lumeau and J. Wenger, *ACS Nano*, 2019, **13**, 8469–8480.
21 J. Eid, A. Fehr, J. Gray, K. Luong, J. Lyle, G. Otto, P. Peluso, D. Rank, P. Baybayan, B. Bettman, A. Bibillo, K. Bjornson, B. Chaudhuri, F. Christians, R. Cicero, S. Clark, R. Dalal, A. deWinter, J. Dixon, M. Foquet, A. Gaertner, P. Hardenbol, C. Heiner, K. Hester, D. Holden, G. Kearns, X. Kong, R. Kuse, Y. Lacroix, S. Lin, P. Lundquist, C. Ma, P. Marks, M. Maxham, D. Murphy, I. Park, T. Pham, M. Phillips, J. Roy, R. Sebra, G. Shen, J. Sorenson, A. Tomaney, K. Travers, M. Trulson, J. Vieceli, J. Wegener, D. Wu, A. Yang, D. Zaccarin, P. Zhao, F. Zhong, J. Korlach and S. Turner, *Science*, 2009, **323**, 133–138.
22 S. Uemura, C. E. Aitken, J. Korlach, B. A. Flusberg, S. W. Turner and J. D. Puglisi, *Nature*, 2010, **464**, 1012–1017.

23 J. Larkin, R. Y. Henley, V. Jadhav, J. Korlach and M. Wanunu, *Nat. Nanotechnol.*, 2017, **12**, 1169–1175.
24 Y. Zhao, D. Chen, H. Yue, M. M. Spiering, C. Zhao, S. J. Benkovic and T. J. Huang, *Nano Lett.*, 2014, **14**, 1952–1960.
25 M. P. Goldschen-Ohm, D. S. White, V. A. Klenchin, B. Chanda and R. H. Goldsmith, *Angew. Chem.*, 2017, **129**, 2439–2442.
26 K. T. Samiee, M. Foquet, L. Guo, E. C. Cox and H. G. Craighead, *Biophys. J.*, 2005, **88**, 2145–2153.
27 T. Miyake, T. Tanii, H. Sonobe, R. Akahori, N. Shimamoto, T. Ueno, T. Funatsu and I. Ohdomari, *Anal. Chem.*, 2008, **80**, 6018–6022.
28 T. Sandén, R. Wyss, C. Santschi, G. Hassaïne, C. Deluz, O. J. F. Martin, S. Wennmalm and H. Vogel, *Nano Lett.*, 2012, **12**, 370–375.
29 J. Chen, R. V. Dalal, A. N. Petrov, A. Tsai, S. E. O'Leary, K. Chapin, J. Cheng, M. Ewan, P.-L. Hsiung, P. Lundquist, S. W. Turner, D. R. Hsu and J. D. Puglisi, *Proc. Natl. Acad. Sci. U. S. A.*, 2014, **111**, 664–669.
30 A. Barik, L. M. Otto, D. Yoo, J. Jose, T. W. Johnson and S.-H. Oh, *Nano Lett.*, 2014, **14**, 2006–2012.
31 D. Garoli, H. Yamazaki, N. Maccaferri and M. Wanunu, *Nano Lett.*, 2019, **19**, 7553–7562.
32 A. B. Dahlin, *Analyst*, 2015, **140**, 4748–4759.
33 T. Auger, J. Mathé, V. Viasnoff, G. Charron, J.-M. Di Meglio, L. Auvray and F. Montel, *Phys. Rev. Lett.*, 2014, **113**, 028302.
34 O. N. Assad, T. Gilboa, J. Spitzberg, M. Juhasz, E. Weinhold and A. Meller, *Adv. Mater.*, 2017, **29**, 1605442.
35 V. Jadhav, D. P. Hoogerheide, J. Korlach and M. Wanunu, *Nano Lett.*, 2019, **19**, 921–929.
36 D. V. Verschueren, S. Pud, X. Shi, L. De Angelis, L. Kuipers and C. Dekker, *ACS Nano*, 2019, **13**, 61–70.
37 K. T. Samiee, J. M. Moran-Mirabal, Y. K. Cheung and H. G. Craighead, *Biophys. J.*, 2006, **90**, 3288–3299.
38 J. Wenger, F. Conchonaud, J. Dintinger, L. Wawrezinieck, T. W. Ebbesen, H. Rigneault, D. Marguet and P.-F. Lenne, *Biophys. J.*, 2007, **92**, 913–919.
39 C. V. Kelly, B. A. Baird and H. G. Craighead, *Biophys. J.*, 2011, **100**, L34–L36.
40 C. V. Kelly, D. L. Wakefield, D. A. Holowka, H. G. Craighead and B. A. Baird, *ACS Nano*, 2014, **8**, 7392–7404.
41 C. I. Richards, K. Luong, R. Srinivasan, S. W. Turner, D. A. Dougherty, J. Korlach and H. A. Lester, *Nano Lett.*, 2012, **12**, 3690–3694.
42 M. Foquet, K. T. Samiee, X. Kong, B. P. Chauduri, P. M. Lundquist, S. W. Turner, J. Freudenthal and D. B. Roitman, *J. Appl. Phys.*, 2008, **103**, 034301.
43 C.-H. Teng, T. A. Lionberger, J. Zhang, E. Meyhöfer and P.-C. Ku, *Nanotechnology*, 2012, **23**, 455301.
44 R. M. Jamiolkowski, K. Y. Chen, S. A. Fiorenza, A. M. Tate, S. H. Pfeil and Y. E. Goldman, *PLoS One*, 2019, **14**, e0222964.
45 A. Degiron, H. J. Lezec, N. Yamamoto and T. W. Ebbesen, *Opt. Commun.*, 2004, **239**, 61–66.
46 J. Wenger, P.-F. Lenne, E. Popov, H. Rigneault, J. Dintinger and T. W. Ebbesen, *Opt. Express*, 2005, **13**, 7035–7044.
47 F. J. García-Vidal, L. Martín-Moreno, E. Moreno, L. K. S. Kumar and R. Gordon, *Phys. Rev. B: Condens. Matter Mater. Phys.*, 2006, **74**, 153411.
48 C. Zhao, Y. Liu, J. Yang and J. Zhang, *Nanoscale*, 2014, **6**, 9103–9109.
49 P. Ponzellini, X. Zambrana-Puyalto, N. Maccaferri, L. Lanzanò, F. D. Angelis and D. Garoli, *Nanoscale*, 2018, **10**, 17362–17369.
50 X. Zambrana-Puyalto, P. Ponzellini, N. Maccaferri, E. Tessarolo, M. G. Pelizzo, W. Zhang, G. Barbillon, G. Lu and D. Garoli, *Chem. Commun.*, 2019, **55**, 9725–9728.
51 D. Molenda, G. C. des Francs, U. C. Fischer, N. Rau and A. Naber, *Opt. Express*, 2005, **13**, 10688–10696.
52 P. Schön, N. Bonod, E. Devaux, J. Wenger, H. Rigneault, T. W. Ebbesen and S. Brasselet, *Opt. Lett.*, 2010, **35**, 4063–4065.
53 G. Lu, W. Li, T. Zhang, S. Yue, J. Liu, L. Hou, Z. Li and Q. Gong, *ACS Nano*, 2012, **6**, 1438–1448.
54 M. Mivelle, T. S. van Zanten, L. Neumann, N. F. van Hulst and M. F. Garcia-Parajo, *Nano Lett.*, 2012, **12**, 5972–5978.
55 E. X. Jin and X. Xu, *Appl. Phys. Lett.*, 2005, **86**, 111106.
56 S. Fore, Y. Yuen, L. Hesselink and T. Huser, *Nano Lett.*, 2007, **7**, 1749–1756.
57 X. Jiao, E. M. Peterson, J. M. Harris and S. Blair, *ACS Photonics*, 2014, **1**, 1270–1277.
58 X. Jiao, Y. Wang and S. Blair, *J. Phys. D: Appl. Phys.*, 2015, **48**, 184007.
59 Y. Wang, E. M. Peterson, J. M. Harris, K. Appusamy, S. Guruswamy and S. Blair, *J. Phys. Chem. C*, 2017, **121**, 11650–11657.
60 A. Barulin, J.-B. Claude, S. Patra, N. Bonod and J. Wenger, *Nano Lett.*, 2019, **19**, 7434–7442.
61 D. Gérard and S. K. Gray, *J. Phys. D: Appl. Phys.*, 2014, **48**, 184001.
62 Y. Kumamoto, A. Taguchi and S. Kawata, *Adv. Opt. Mater.*, 2019, **7**, 1801099.
63 M. W. Knight, N. S. King, L. Liu, H. O. Everitt, P. Nordlander and N. J. Halas, *ACS Nano*, 2014, **8**, 834–840.
64 K. M. McPeak, S. V. Jayanti, S. J. P. Kress, S. Meyer, S. Iotti, A. Rossinelli and D. J. Norris, *ACS Photonics*, 2015, **2**, 326–333.
65 J. de Torres, P. Ghenuche, S. B. Moparthi, V. Grigoriev and J. Wenger, *ChemPhysChem*, 2015, **16**, 782–788.
66 S. Patra, M. Baibakov, J.-B. Claude and J. Wenger, *Sci. Rep.*, 2020, **10**, 5235.
67 S. Kühn, G. Mori, M. Agio and V. Sandoghdar, *Mol. Phys.*, 2008, **106**, 893–908.
68 I. Berlman, *Handbook of florescence spectra of Aromatic Molecules*, Academic press, 2nd edn, 1971.
69 T. Kohl and P. Schwille, in *Microscopy Techniques*, ed. J. Rietdorf, Springer Berlin Heidelberg, Berlin, Heidelberg, 2005, pp. 107–142.
70 J. Widengren and Ü. Mets, in *Single Molecule Detection in Solution*, John Wiley & Sons, Ltd, 2003, pp. 69–120.
71 M. N. Polyanskiy, *Refractive index database*, https://refractiveindex.info, accessed July 19, 2019.

